 doi:10.20944/preprints202101.0586.v1

Article

Optimization of the obtaining of cellulose nanocrystals from *Agave tequilana* Weber var. Azul bagasse by acid hydrolysis

Manuel Alberto Gallardo-Sánchez [1], Tania Diaz-Vidal [2], Alejandra Berenice Navarro-Hermosillo [1], Edgar Benjamín Figueroa-Ochoa [3], Rogelio Ramírez Casillas [4], José Anzaldo Hernández [4], Luis Carlos Rosales-Rivera [2], J. Felix Armando Soltero Martínez [2], Salvador García Enríquez [4], Emma Rebeca Macías-Balleza [2,*]

[1] Departamento de Ingeniería de Proyectos, Centro Universitario de Ciencias Exactas e Ingenierías, Universidad de Guadalajara, Guadalajara, Mexico; manuel.gallardo@academicos.udg.mx, alenicenavarro@gmail.com.

[2] Departamento de Ingeniería Química, Centro Universitario de Ciencias Exactas e Ingenierías, Universidad de Guadalajara, Guadalajara, Mexico; taniadzv@hotmail.com, carlos.rosales@academicos,udg.mx, armando.soltero@academicos.udg.mx,

[3] Departamento de Química, Centro Universitario de Ciencias Exactas e Ingenierías, Universidad de Guadalajara, Guadalajara, Mexico; benjamin.figueroa@academicos.udg.mx

4 Departamento de Madera Celulosa y Papel, Centro Universitario de Ciencias Exactas e Ingenierías, Universidad de Guadalajara, Guadalajara, Mexico; roramire@gmail.com, j.anzaldo@academicos.udg.mx, salgaren@hotmail.com

* Correspondence: emma.macias@academicos.udg.mx; Tel.: 52 33 13 78 59 00 (27591).

Abstract: A multilevel factorial design of 2^3 with 12 experiments was developed for the preparation of cellulose nanocrystals (CNC) from *Agave tequilana* Weber var. Azul bagasse, which is an agroindustrial waste from Tequila production. The studied parameters were acid type (H_2SO_4 and HCl), acid concentration (60 and 65 wt% for H_2SO_4, 2 and 8N for HCl) temperature (40 and 60°C for H_2SO_4, 50 and 90°C for HCl), and hydrolysis time (40, 55 and 70 min for H_2SO_4, 30, 115 and 200 min for HCl). The obtained CNC were physical and chemically characterized using dynamic light scattering (DLS), atomic force microscopy (AFM), Fourier-transform infrared spectroscopy (FT-IR), X-ray photoelectron spectroscopy (XPS), and X-ray diffraction (XDR) techniques. The size and morphology of *A. tequilana* CNC strongly depend on the acid type and hydrolysis parameters. The shortest CNC were obtained with H_2SO_4 (65 wt%, 40 °C, and 70 min) had a length of 137 ± 68 nm, width 33 ± 7 nm, and height 9.1 nm, whereas the shortest CNC obtained with HCl (2 N, 50 °C and 30 min) had a length of 216 ± 73 nm, width 69 ± 17 nm, and height 8.9 nm. CNC prepared from H_2SO_4 resulted shorter and thinner than those obtained with HCl. The total sulfate groups content in CNC obtained with H_2SO_4 increase with time agree to $C_{SG} = ae^{bt}$, and increases with temperature and acid concentration.

Keywords: *Agave tequilana*; bagasse; cellulose nanocrystals; acrylic hydrolysis; AFM; factorial design

1. Introduction

Cellulose nanocrystals (CNC) are highly crystalline nanoparticles shaped like an elongated bar, with diameters between 2-20 nm, and lengths of <500 nm [1,2]. CNC have desirable physical, chemical, and mechanical properties, such as an elastic modulus around 150 GPa, which is greater than the elastic modulus of glass fibers (85 GPa) and aramid (65 GPa) [3–5], high tensile strength (7500 MPa), high stiffness (Young's modulus ≥140 GPa), a high surface area, high aspect ratio, an abundance of surface hydroxyl groups available for easy chemical modifications, and full biodegradability, due to its

Preprints (www.preprints.org) | NOT PEER-REVIEWED | Posted: 28 January 2021 doi:10.20944/preprints202101.0586.v1

natural origin [1–4,6]. Therefore, CNC have been used as reinforcing materials to improve the mechanical properties of composites in multiple applications, such as plastics, ceramics, concrete, etc. [7].

Typically, CNC are obtained through the removal of the amorphous cellulose regions by chemical means [3,6]. The prior purified cellulose material is subjected to hydrolysis with a strong acid under strictly controlled conditions, followed by dialysis in water and successive washes to remove the free acid. Usually, an extra step with ultrasound and filtration is considered to separate residues and ensure a stable colloidal suspension [5,8,9]. The amorphous regions in the cellulose chains are more susceptible to acid hydrolysis than crystalline regions, thus the breakdown of glycosidic bonds is facilitated, releasing the individual crystals. H_2SO_4 and HCl are frequently used for the preparation of CNC, however phosphoric and hydrobromic acids have been regularly employed [10]. The most studied parameters for acid extractions with H_2SO_4 include hydrolysis times from 40-70 min, temperatures ranging from 40-60°C and acid concentrations between 60-65 wt% [9–15]. In the case of HCl the most used conditions are 30-200 min, 60-110°C, and concentrations from 2-8 N for HCl [16–19].

Agave tequilana Weber var. Azul is the main resource from the tequila industry. To obtain a liter of tequila, *A. tequilana* heads are cooked, crushed, and sugar extracted, to finally generate approximately 1.4 kg of bagasse in wet weight. According to the Tequila Regulatory Council, 490,000 tons of bagasse from, all *A. tequilana* varieties, were obtained in the process of tequila generation solely in 2019, of which 290,500 tons corresponded to the *A. tequilana* Weber var. Azul [20]. The excess bagasse creates an enormous environmental impact in terms of agro-waste management and disposal by tequila industries [21]. Extensive effort has focused on the comprehensive use of *A. tequilana* bagasse in the last years. Many studies point to the high cellulose content of *A. tequilana* bagasse, close to 80% [22,23], as the main source for the production of high-added value subproducts, such as cellulose nanocrystals [24].

Depending on the cellulose raw material, pretreatment, and hydrolysis process, CNC with tunable properties can be obtained [25]. CNC extracted with HCl show poor colloidal stability, whereas CNC produced with H_2SO_4 form highly stable colloidal dispersions due to electrostatic repulsion caused by negatively charged sulfate ester groups on their surface and lower thermal stability [26]. Increasing temperatures and reaction times have been associated with smaller nanocrystal sizes; however, severe reaction conditions can reduce the yield and shorten the crystal size [13,27]. Thus, a comprehensive study analyzing acid concentration and determining the best operational output is mandatory to universally optimize the obtaining of CNC. In this sense, the design of a factorial experiment can be employed to optimize the process of CNC production from *A. tequilana* bagasse. The design aims to determine if the principal factors are statistically significant based on a null hypothesis test, with a confidence value of $p < 0.05$ [16,28]. Compared to one-factor-at-a-time experiments, factorial designs allow the detection and study of interactions in a more efficient way [29]. This technique has already been employed to optimize the isolation and production of microcrystalline and nanocrystalline cellulose from recycled wood pulp [30], *Picea abies* [31], and *Acacia farnesiana L. Willd* bagasse [32] with a reduced number of experiments, time, and cost.

In the present work, two multilevel factorial 2^3 experimental designs were selected to optimize the process of CNC isolation from *A. tequilana* by acid hydrolysis with H_2SO_4 and HCl respectively. The principal factors were acid concentration, reaction time, and temperature. To determine the best operational conditions and if they are statistically significant, CNC length measured by AFM, reaction yield and, sulfate groups in CNC-S were analyzed; while AFM width and height, DLS, FTIR, and XRD were used to characterize the obtained CNC.

2. Materials and Methods

Preprints (www.preprints.org) | NOT PEER-REVIEWED | Posted: 28 January 2021 doi:10.20944/preprints202101.0586.v1

2.1 Materials

Bagasse from *A. tequilana* Weber var. Azul was kindly donated by Mundo Agave (Tequila, Jalisco, Mexico). Sulfuric acid (H_2SO_4, 97 wt%) and hydrochloric acid (HCl, 37 wt%) were obtained from Golden Bell (Mexico). Dialysis membranes Spectra/Por 4 MWCO 12-14 KDa were purchased from Thomas-Scientific (Swedesboro, NJ, USA). Filters were provided by Thermo Fisher Scientific (Waltham, MA, USA). All solutions were prepared using milli-Q water with a resistivity of 10 MegOhm.cm at 25°C.

2.2 Experimental design

The multilevel factorial designs of 2^3 were developed via STATGRAPHICS Centurion XVI (The Plains, VA, USA) to investigate the effect of acid concentration, hydrolysis time and, temperature in the final length measured using AFM and yield of CNC produced from *A. tequilana* Weber var. azul. The experimental factor details are described in Table 1 and the detailed list of controllable process factors is shown in Table 2. CNC obtained using H_2SO_4 hydrolysis will be denoted as CNC-S and HCl hydrolysis as CNC-H.

Table 1. Controllable process factors and their respective levels for CNC acid hydrolysis length optimization.

	H_2SO_4			HCl		
	-1	**0**	**+1**	**-1**	**0**	**+1**
Concentration	60 wt%	-	65 wt%	2 N	-	8 N
Temperature (°C)	40	-	60	50	-	90
Time (min)	40	55	70	30	115	200

Table 2. Multilevel factorial design 2^3 process factors for CNC acid hydrolysis length optimization.

H_2SO_4				HCl			
Sample	**Conc. (wt%)**	**T (°C)**	**t (min)**	**Sample**	**Conc. (N)**	**T (°C)**	**t (min)**
E1S	60	40	40	**E1H**	2	50	30
E2S	65	40	40	**E2H**	8	50	30
E3S	60	60	40	**E3H**	2	50	200
E4S	65	60	40	**E4H**	8	50	200
E5S	60	40	70	**E5H**	2	90	30
E6S	65	40	70	**E6H**	8	90	30
E7S	60	60	70	**E7H**	2	90	200
E8S	65	60	70	**E8H**	8	90	200
E9S	60	40	55	**E9H**	2	50	115
E10S	65	40	55	**E10H**	8	50	115
E11S	60	60	55	**E11H**	2	90	115
E12S	65	60	55	**E12H**	8	90	115

2.3 Preparation of cellulose nanocrystals

Soluble-grade cellulose pulp from *A. tequilana* was obtained according to Gallardo-Sánchez et al. [22]. Briefly, soluble-grade cellulose was ground with an IKA MF 10 mill (Staufen, Germany) until particles of 0.5 mm mesh. The hydrolysis was carried out with variable conditions of concentration, temperature, and time (Table 2), with 12 different conditions for each acid. The acidic solutions were prepared and poured into a three-necked reactor with a capacity of 1 L, then, the solution was heated to the working temperature in an isothermal Haake bath C1 (Vreden, Germany), with a mechanical stirrer RZR 50 Caframo (Ontario, Canada) at 300 rpm. Next, 20 g of soluble- grade cellu-

Preprints (www.preprints.org) | NOT PEER-REVIEWED | Posted: 28 January 2021 doi:10.20944/preprints202101.0586.v1

lose (dry base) was added during the corresponding time. A ratio of 10:1 (v/w) and 30:1 (v/w) was used for the hydrolysis with H_2SO_4 and HCl, respectively.

After the hydrolysis reaction, the CNC solution was poured into deionized water at 4°C, centrifuged (5000 rpm for 45 min), and the precipitates were dialyzed in deionized water (12-14 KDa) at room temperature until the pH reached 5.5. The water was replaced every 12 h. The CNC were then sonicated for 8 min in an Elma ultrasound bath model TI-H-15 (Singen, Germany), filtered through 2, 1.5, and 1 μm filters, and stored at 4°C until further use.

2.4 Determination of sulfate groups in CNC-S

The residual concentration of sulfate groups on the CNC-S surface (mmol/kg) was measured using a Thermo Fisher Scientific Orion Star A211 potentiometer (Waltham, MA, USA). Titration of sulfate groups (C_{SG}) was performed using 0.05 N NaOH and 30 mL of a CNC-S solution in 150 mL of deionized water in a 3-neck flask. The analysis of the samples started by adding 0.5-1 mL of NaOH to the CNC suspension at constant stirring. pH and conductivity values were recorded until no further variations were detected. The conductivity *vs* NaOH volume plot shown two tendencies, so two slope lines were drawn, the intercept of both was located and V_2 was determined and the ionizable groups were calculated as follows:

$$C_{SG} = Ct * \frac{V_2}{m} \quad (1)$$

Where C_{SG} is the total sulfate groups content in *mmol/kg*, *Ct* is the NaOH concentration, in this case, 0.05 N, V_2 is the NaOH consumed volume in ml and *m* is the dried mass of the CNC-S in *g*.

2.5 X-ray photoelectron spectroscopy (XPS)

XPS which is a quantitative analysis method, measures the energy of excited electrons with an X-ray beam, at the lowest energy levels. This technique is performed within the first 10 nm of the surface and allows to identify elements, except H and He, in atomic concentrations greater than 0.1%, determining the elemental composition of the surface with an error of less than 10% [33]. The equipment possesses an X-ray source, Al kα XR5 (hν = 1486.7 eV), and a Phoibos detector with hemispherical Thermo Fisher Scientific Alpha 110 spectrometer (Waltham, MA, USA).

2.6 Fourier-transform infrared spectroscopy (FTIR)

FTIR measurements were performed with a Perkin-Elmer Spectrum GX (Waltham, MA, USA) in ATR mode. The spectra of powdered CNC were obtained by recording 16 scans at a resolution of 4 cm^{-1}, and a frequency range from 4,000 to 700 cm^{-1}.

2.7 X-ray diffraction (XRD)

CNC were analyzed with a Malvern Instruments XRD Empyrean (Malvern, UK) with Cu-Kα radiation at 45 kV and a current of 40 mA. The incidence angle was set to 5-70° (step size of 0.2°). The percentage of crystallinity was calculated according to the Rietveld method [34], and the data was analyzed with the University of Trento MAUD 2.1 software (Trento, Italy).

2.8 Atomic force microscope (AFM)

The morphology of CNC was characterized using a Park Systems AFM NX10 (South Korea). A solution of CNC (0.005%, in water) was transferred to a metal microscope slide and air-dried. CNC images were obtained via tapping mode in the air using Budget Sensors Tap300-G probe (Izgrev, Sofia, Bulgaria). For most images, at least 30 CNC were measured and the AFM dimensions reported are the CNC length (L), height (H), and width (W).

2.9 Dynamic light scattering (DLS) and Z-potential

Preprints (www.preprints.org) | NOT PEER-REVIEWED | Posted: 28 January 2021 doi:10.20944/preprints202101.0586.v1

The average size and polydispersity index (PdI) of CNC were measured using a dynamic light scattering (DLS) form Malvern Instruments Zetasizer Nano Series ZS90 (Malvern, UK). CNC solutions were first sonicated in an Elma P120H ultrasound bath (Singen, Germany), at a frequency of 40 kHz and 30% power, at room temperature, for 30 minutes. Subsequently, the second dilution of CNC was made (1:10 ratio) and sonicated again for 10 minutes. Between 6 and 18 scans were made for each sample and each scan is the average of 10 repetitions, the statistical average is reported. The selected DLS parameters were refractive index (RI = 1.3) and absorption (0.01). Z-potential measurements were made using the same diluted samples prepared for DLS (E1S and E1H), but using a disposable capillary cell (DTS1070).

3. Results

3.1. Yield and Factorial design

CNC of *A. tequilana* bagasse were prepared using 24 experimental acid hydrolysis conditions (12 conditions with H_2SO_4 and 12 conditions with HCl) (Table 2). The maximum CNC yields obtained were 96% and 90% for experimental conditions E8S and E8H, respectively. The minimum CNC yields were observed with the experimental conditions E1S and E1H, with values of 4.2% and 4.5%, respectively. The standardized Pareto plots for both CNC yields, exhibits that not a single factor or interaction between factors is statistically significant as shown in Figure S1. The complete list of obtained yields for all experimental are shown in Tables S1 and S2 for HCl and H_2SO_4 respectively.

3.2. Determination of sulfate groups in CNC-S

Figure 1a shows the total sulfate groups, *i.e.* the residual charge of H_2SO_4 on the CNC-S surface, as a function of hydrolysis time for all H_2SO_4 hydrolysis experiments. The total content of sulfate groups (C_{SG}) increased with time, temperature, and acid concentration, exhibiting an exponential behavior of $C_{SG} = ae^{bt}$. The "a" and "b" equation values are shown in Table 3.

Table 3. Total sulfate groups content equation parameters.

T(ºC) / [H_2SO_4] (wt%)	40			60		
	a *(mmol/kg)*	**b** *(1/min)*	**R^2**	***a*** *(mmol/kg)*	**b** *(1/min)*	**R^2**
60	1.90 ± 0.84	0.04 ± 8x10^{-3}	0.8976	1.46 ± 0.69	0.07 ± 8x10^{-3}	0.9446
65	1.95 ± 0.13	0.01 ± 1x10^{-3}	0.9983	5.38 ± 0.015	0.05 ± 5x10^{-5}	1.0

The principal factors and factor interactions with higher influence are shown in the Pareto diagram (Figure 1b). Positive effects indicate an increase from the minimum level to the maximum, while negative effects implies the opposite [35]. Concentration, time, and temperature are statistically significant ($p < 0.05$) factors contributing to the increase in C_{SG}. The highest amount of sulfate groups was quantified for experimental conditions E7S (162.0 mmol/kg) and E8S (166 mmol/kg). The complete list of total sulfate groups content is shown in Tables S3. Our results are similar to those obtained for other source, such as huizache wood (39.78 mmol/kg with 65% H_2SO_4, 45°C and 45 min reaction, and 26.9 mmol/kg with 60% H_2SO_4, 55°C and 65 min of reaction) [27]. Interactions BC (time and temperature) and CC (quadratic time) were also statistically significant ($p < 0.05$), and had a positive effect.

Preprints (www.preprints.org) | NOT PEER-REVIEWED | Posted: 28 January 2021 doi:10.20944/preprints202101.0586.v1

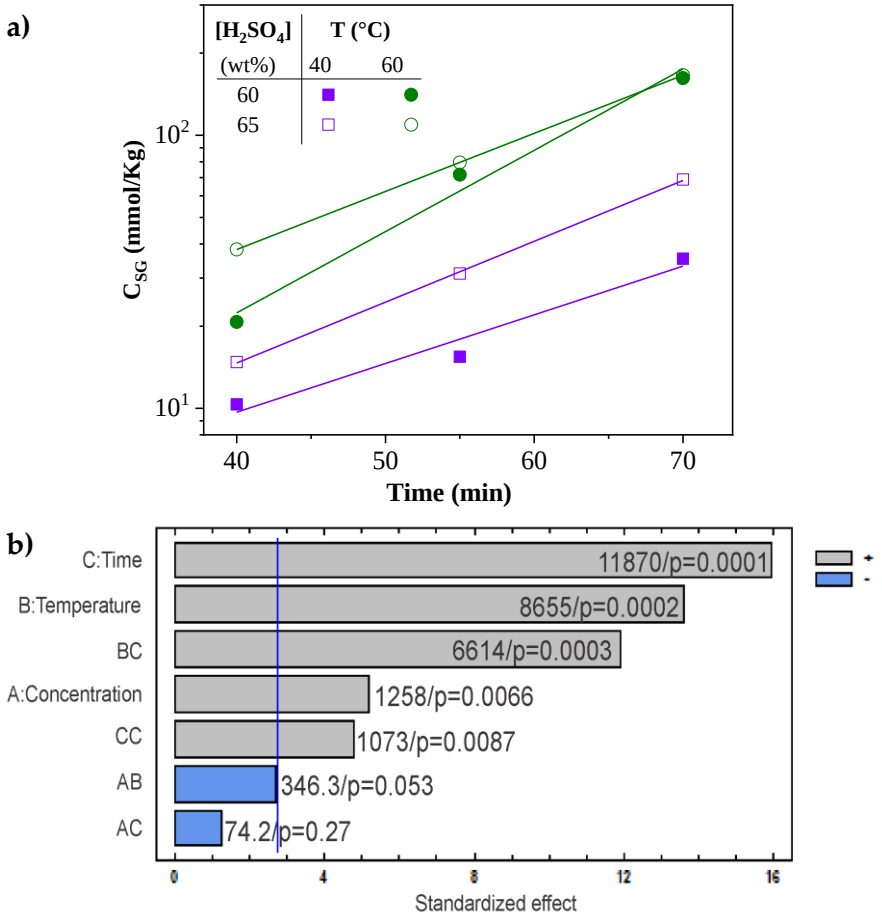

Figure 1. (**a**) Total sulfate groups content (C_{SG}) as a function of time, for different temperatures and H_2SO_4 concentrations. The lines represent the exponential equation: $C_{SG} = ae^{bt}$. (**b**) Standardized Pareto diagram for total sulfate groups present in CNC-S, the sum of squares and the p value are shown at the right side of each bar.

3.3. X-ray photoelectron spectroscopy (XPS)

Soluble-grade cellulose pulp and CNC-S were analyzed by XPS before and after acid hydrolysis at the lower limit condition tested (E1S). In the inspection spectrum of soluble-grade cellulose and CNC-S (Figure 2a,b), the main peaks are located at 285 and 532 eV, corresponding to C and O atoms, respectively. In the case of CNC-S, there is the presence of an S atom peak at 164 eV, which is obtained during H_2SO_4 hydrolysis.

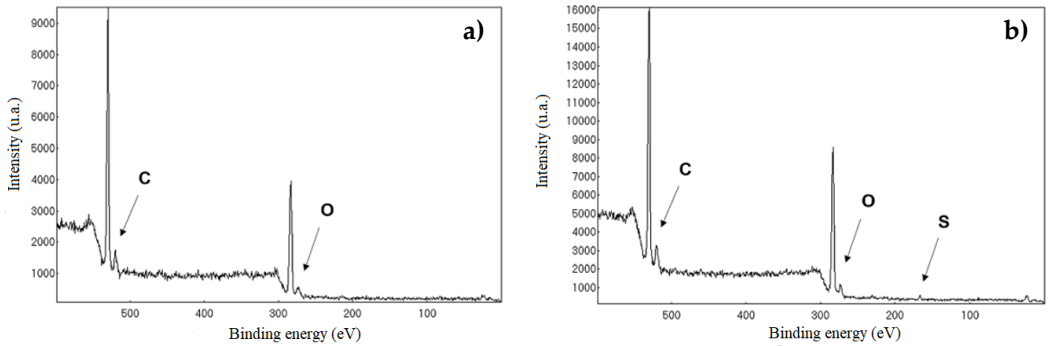

Figure 2. XPS spectrum of (**a**) soluble-grade cellulose pulp, and (**b**) CNC-S (Sample E1S).

The spectra deconvolution were performed for C1s, O1S for soluble-grade cellulose (Figure 3a,b), and C1s, O1s, and S2p for CNC-S (Figure 3c,d,e). In the high resolution C1s spectra, the C signal is resolved into three distinctive peaks for both soluble cellulose and

Preprints (www.preprints.org) | NOT PEER-REVIEWED | Posted: 28 January 2021 doi:10.20944/preprints202101.0586.v1

CNC-S, with bond energies at 283, 285 and, 288 eV, attributed to C-C, C-O, C-OH, and C-O-C bonds, respectively. In the high resolution O1s spectra, two peaks were observed at 532 and 533 eV, attributed to O-H and O-C bonds for soluble cellulose spectra. In the O1s spectra of CNC, these signals were resolved at peaks 533 and 534 eV, due to the presence of S atoms [33]. Due to this shift, the S-O bond is located at a binding energy of 169 eV for S2p.

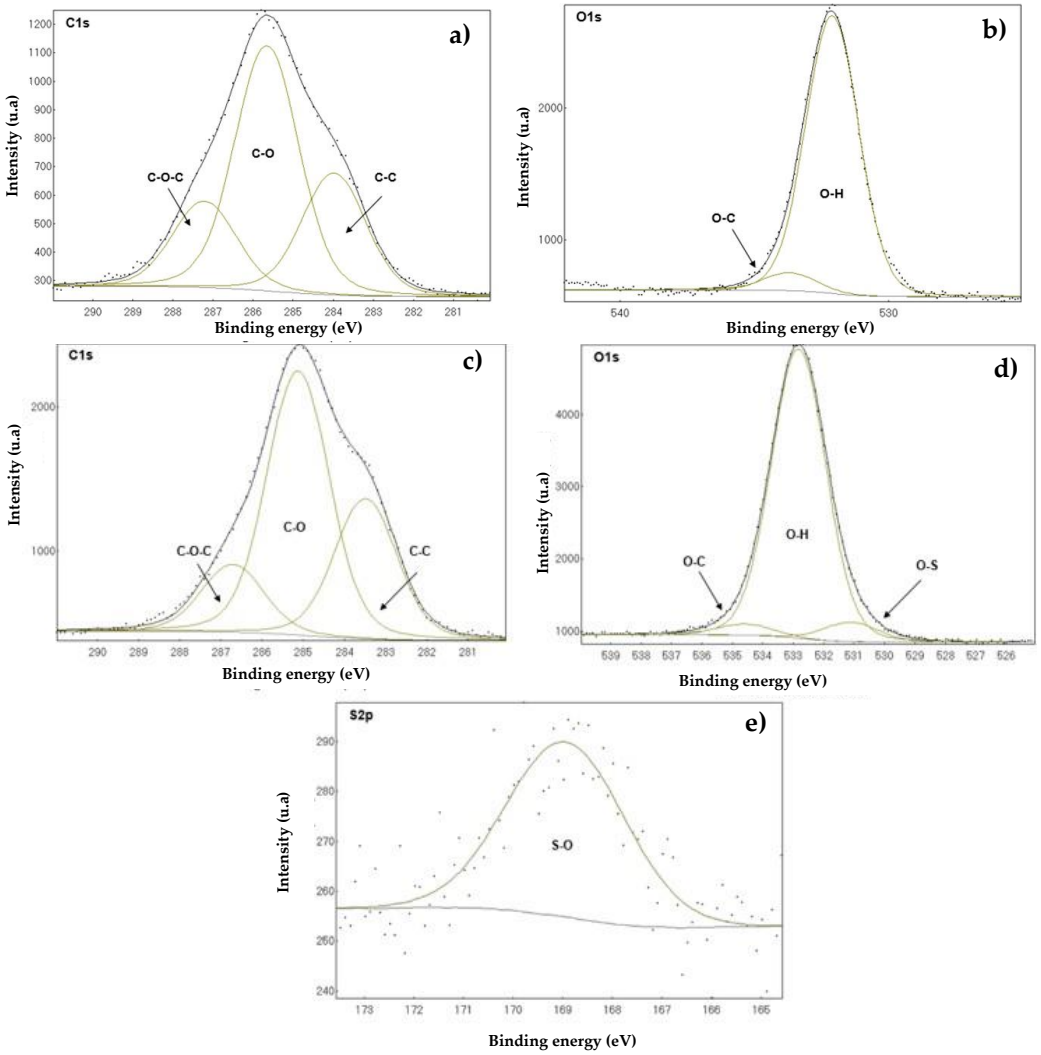

Figure 3. High resolution spectra for soluble-grade cellulose pulp: (**a**) C1s, (**b**) O1s, and CNC-S: (**c**) C1S, (**d**) O1s, and (**e**) S2p.

Table 4 shows the atomic composition of soluble-grade cellulose pulp and CNC-S. After hydrolysis, the total SO_4 group content of CNC-S was 4.92 wt%. The stoichiometry of the sample could not be determined, as the H atom was not detected by the XPS technique. However, the total percentage of O atoms was higher compared to soluble-grade cellulose due to an increase in OH bond formation. The values obtained in the analysis of soluble-grade cellulose pulp (α-cellulose) are similar to the results depicted at the database of the natural polymers manual [36], in where two components for C1s are reported, with binding energies of 286.73 and 288.06 eV for the C-C and C-O bonds, respectively. For O1s spectra, two components at 532.93 eV for the O-H bond, and 533.51 eV for the C-O are detailed.

Table 4. Atomic composition of soluble-grade cellulose pulp and CNC (E1S) by XPS.

Sample	Soluble-grade cellulose pulp	CNC (E1S)

Preprints (www.preprints.org) | NOT PEER-REVIEWED | Posted: 28 January 2021 doi:10.20944/preprints202101.0586.v1

Z		C	Atom %	Atom %	C	Atom %	Atom %
	C-O-C	4.51	10.96		5.63	7.58	
C1s	C-O, C-OH	12.89	31.32	57.82	23.58	31.72	56.12
	C-C	6.40	15.54		12.50	16.82	
	O-H	15.44	37.49		25.74	34.63	
O1s	O-C	1.93	4.69	42.18	1.90	2.56	38.96
	O-S	-	-		1.31	1.77	
S2p	S-O	41.17	100	0	3.66	4.92	4.92
Total		41.17	100	100	74.33	100	100

3.4. Fourier-transform infrared spectroscopy (FTIR)

Figure 4 shows the comparison of the spectra of soluble-grade cellulose pulp and CNC-S (E10S) and CNC-H (E3H). The obtained spectra showed characteristic frequencies of cellulose, where the vibration bands of C–H bonds (2918 cm^{-1} [asymmetric vibrations], 2851 cm^{-1} [symmetric vibrations]), and C–H bonds (1360 and 1318 cm^{-1} [crystal band] [37,38]) were observed, the latter being an indicator of the presence of CNC, as the band is associated with the preferential directional arrangement of α-cellulose. Bands corresponding to C–O bonds (1054 and 1030 cm-1) are observed, whereas those at frequencies of 1160 cm^{-1} are due to asymmetric vibrations (C–O–C bonds), and O–H bonds (broadband between 3600 and 3200 cm^{-1}, as well as bands at 1335 and 1205 cm^{-1}). The vibration of the anomeric carbon group of the carbohydrate C^1–H is observed at 898 cm^{-1} and at 1635 cm^{-1} the band corresponding to adsorbed water [18,39,40].

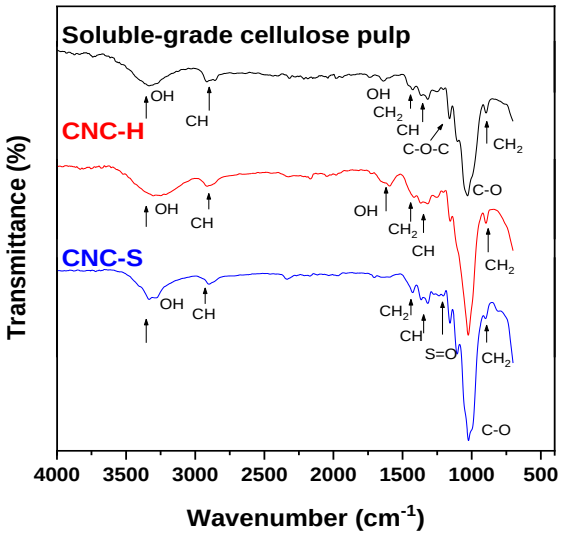

Figure 4. FTIR spectra comparison for soluble-grade cellulose pulp, CNC-H (E10H) and CNC-S (E3S).

The CNC-S spectrum shows a weak sulfur peak at 1202 cm^{-1}, which does not appear in the FTIR spectrum of soluble-grade cellulose pulp. This peak is associated with S=O bonds indicating esterification of the hydroxyl groups during acid hydrolysis. On the other hand, a band corresponding to chlorine ions was not observed for CNC-H, indicating that the hydrolysis with HCl results in hydroxyl groups, which are also present in the soluble-grade cellulose pulp [14,16]. The less intense peak located in the region between 3400 and 3200 cm^{-1} indicates the crystallinity of both CNC, since the hydrogen bond is less flexible in the crystalline structure [17,41,42].

The sensitive region in FTIR for the detection of the crystallinity of cellulosic materials is located between 850 and 1500 cm^{-1} [41]. The order index is defined by Oconor *et al.* [41] as the absorbance ratio of the bands detected at wavelengths of 6.9 and 11 μ (1430 and 900 cm-1, known as crystalline and amorphous bands of cellulose) corresponding to vibrations of CH_2, the symmetric and rolling bending, respectively and is defined as LOI: A_{1430}/A_{900} [41,43–48]. The absorbance ratio of 1363 and 2907 cm^{-1} is attributed to the flex-

Preprints (www.preprints.org) | NOT PEER-REVIEWED | Posted: 28 January 2021 doi:10.20944/preprints202101.0586.v1

ural and stretching vibrations of C-H bonds. This relationship is known as the total crystallinity index (TCI: A_{1363}/A_{2907}) [45,48–50]. The hydrogen bonding intensity is reported by several authors [43,44,46,51] as the ratio A_{3350}/A_{1337}. The lateral (LOI) and total (TCI) crystallinity indices, as well as the hydrogen bond intensity (HBI) for soluble-grade cellulose were 1.04, 1.06, and 0.87 respectively. As reference, for Whatman paper the values were 1.21, 0.89 and 0.99. For CNC-S and CNC-H samples (E1S, E8S, E10S, E3H, and E8H) LOI and TCI values of 1.03 ± 0.17 and 1.00 ± 0.13 were obtained, similar to those of soluble cellulose, and HBI values of 1.14 ± 0.1, slightly bigger than that of soluble-grade cellulose pulp. These values were not related to acid nor hydrolysis conditions and were different than those reported for CNC-S obtained from sugar cane bagasse (LOI: 0.57, TCI: 1.32) [45].

3.5. X-ray diffraction (XRD)

Figure 5 shows the diffractograms of the soluble-grade cellulose pulp, CNC-H and CNC-S. Peaks at 2θ angles for the 3 spectra are similar to the reported in the literature for cellulose crystalline allomorphs [18] with main signals at 2θ = 14.5° (1 0 1), 16.5° (1 0 -1), 22.4° (0 0 2) and 34.8° (0 4 0) [52]. The curves showed peaks associated with cellulose corresponding to the crystalline planes, which are present in all cases with different intensity and broadening. A very common assumption is that the increased amorphous region contribution is the main source of peak broadening [38]. However, several factors may influence peak broadenings, such as anisotropy and nanocrystal size [53]. This could explain the peak 22.4°, peak for CNC-S and CNC-H, where a slight broadening can be observed at the beginning, which is not observed in the spectra of soluble-grade cellulose pulp.

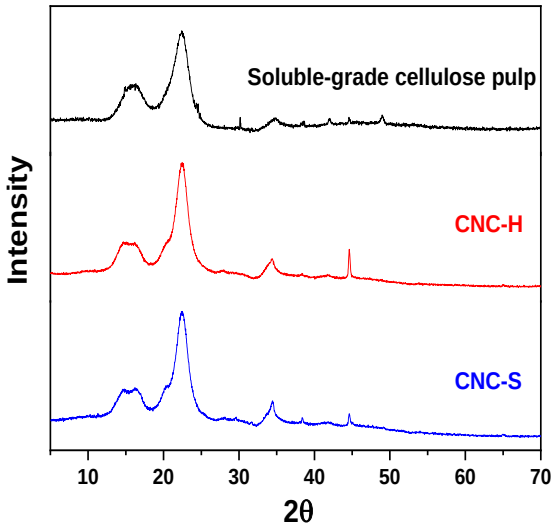

Figure 5. XRD spectra comparison for soluble-grade cellulose pulp, CNC-H (E10H) and CNC-S (E3S).

The crystallinity percentages were calculated with the Rietveld method [34] (Figure S2). The crystallinity values for CNC were recorded for samples E1S (88.4%), E8S (91.3%), and E10S (89.7%), whereas the crystallinity value for CNC-H was recorded for sample E3H (90.1%). Compared to a previous work developed by our research group, a crystallinity value of 79.2% was obtained from soluble-grade cellulose pulp [22]. The values herein reported are higher than those found in the literature for Avicel® PH-102 (51%) [54], Kraft eucalyptus dry lap pulp (73%, H_2SO_4 concentration of 58 wt.%) [55], and *A. tequilana* (TEMPO/NaOCl/NaBr system, 78.5%) [56].

3.5. Atomic force microscopy (AFM)

AFM measurements were carried out to measure the length (L), height (H), and width (W) of dry deposited CNC-H and CNC-S.

Preprints (www.preprints.org) | NOT PEER-REVIEWED | Posted: 28 January 2021 doi:10.20944/preprints202101.0586.v1

The CNC-H morphology is affected by the hydrolysis conditions, as can be seen in Figure 6 where can be observed AFM images of CNC-H for 2D and height histogram for E1H and E8H, respectively (Figure 6a,b), and their 3D projection (Figure 6c,d). The images show the presence of long, wide, and non-homogenous crystals, with an average H for the mildest and more severe hydrolysis conditions.

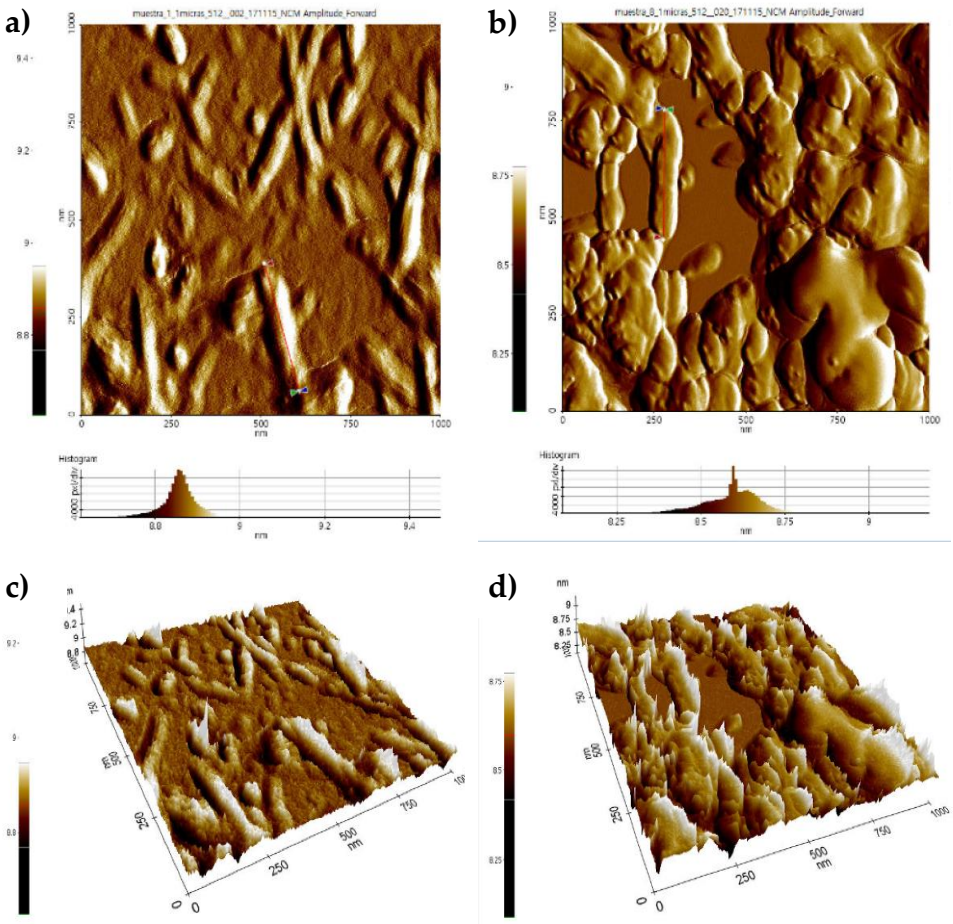

Figure 6. AFM images of CNC-H for two different conditions: (**a**) 2D image and histogram of E1H, (**b**) 2D image and histogram of E8H, (**c**) 3D image of E1H, (**d**) 3D image of E8H.

The average lengths are 263 ± 73 and 266 ± 107 nm for both samples respectively, while the H are similar, 8.9 and 8.6 nm. It is evident that for the mildest conditions, the CNC-H are thinner than those obtained for most severe conditions. The values of L and W were measured from all CNC-H AFM images, while the equipment software provides the CNC height. The complete set of AFM images of CNC-H are shown in Figure S3 and the statistical average dimensions obtained from the CNC-H images at different concentrations, temperatures, and hydrolysis times are depicted in Table S4, likewise, the aspect ratios L/W, L/H, and W/H are also reported.

The results show the CNC-H length diminishes as the HCl concentration increases, the average L for HCl 8N is 322 ± 38 nm, except for sample E2H, for which the length is 829 ± 282 nm, while when the acid concentration is 2N, L tends to increase with temperature and hydrolysis time, ranging from 200 to 800 nm. Most of the samples exhibit W between 60 and 110 nm and the average H is 8.9 ± 0.2 nm. For the 12 samples, the aspect ratios L/W and W/H are 5.4 ± 3.1 and 11 ± 6 nm respectively. The L/H ratios for CNC-H obtained with 2N HCl tend to increase with temperature and time, with values ranging from 20 to 98 nm, whereas L/H aspect ratio values for 8N HCl are in the range of 30 to 40, except for the E2H sample.

Preprints (www.preprints.org) | NOT PEER-REVIEWED | Posted: 28 January 2021 doi:10.20944/preprints202101.0586.v1

When W and H values are similar CNC have a cylindrical shape with a circular cross-section, however, our results show that the cross-section of the nanocrystals is wider than it is high, which may correspond to an elliptical shape, discarding the rectangular cross-section since different heights are observed for a single particle and not a constant height in all the samples analyzed, as can be seen in Figure 6, Figure S3 and Table S4. The CNC-H morphology may be due to a certain degree of agglomeration of the particles since there are no grafted groups on its molecules to stabilize CNC-H solutions [27]. A complete comparison of CNC-H with different raw materials is shown in Table 5. The L/D aspect ratio reported in this work is based on the CNC height. It is worth mentioning that there is no information yet in the CNC literature obtained from *A. tequilana* by hydrolysis with HCl.

Table 5. Length and diameter comparison of CNC-H from different raw sources

Source	Conditions	Diameter (nm)	Length (nm)	L/D	Reference
***Agave tequilana* Weber var. azul bagasse**	All	8.6-9.1	216-829	29.9-95.2	This work
	E1H (2N, 50ºC, 50 min)	8.9	216	29.9	
	E8H (8N, 90ºC, 115min)	8.6	266	30.9	
MCC	4N, 80ºC, 225 min	10 - 20	-	-	[57]
MCC	8N, 110ºC, 180 min	14 - 16	200 - 250	14 - 15	[18]
MCC	6N, 110ºC, 180 min	10 - 30	190 - 250	10 - 25	[16]
***Acacia farnesiana* L. Willd**	2-8 N, 50-90 ºC, 30-200 min	-	100-512	-	[27]

AFM images of CNC-S for 2D and height histogram for E1S and E8S (Figure 7a,b), and their 3D projection (Figure 7c,d) showed the presence of thin, ellipsoidal nanocrystals, with L of 404 and 149 ± 59 nm respectively for mildest and more severe hydrolysis conditions. The H and W are similar, with a W/H aspect ratio (4 ± 0.5 and 4.5 ± 1.3 nm respectively). The complete set of AFM images of CNC-S are shown in Figure S4 and the AFM dimensions obtained from AFM images are presented in Table S5. H is constant with an average value of 9.1 ± 0.3 nm for the 12 experiments.

The CNC-S morphology is affected by the hydrolysis conditions, the average length decreases with increasing time in the hydrolysis process for the different temperatures and acid concentrations, and, at the same time, the width is affected similarly, obtaining thinner crystals as the hydrolysis time increases, regardless of the acid concentration or the treatment temperature. For example, in Figure S4, for 65% acid at 40°C, as the hydrolysis time increases, the CNC-S width tends to decrease, presenting values of 73 ± 11 nm, 49 ± 18 nm, and 33 ± 7 nm at 40, 55, and 70 minutes respectively ($W_{E2S} > W_{E10S} > W_{E6S}$). A similar pattern was also observed for H_2SO_4 60 wt% at 40°C ($W_{E1S} > W_{E9S} > W_{E5S}$). The effect is also observed with increasing temperature from 40 to 60°C, for example for 65% acid and 55 minutes, the width diminished from 49 ± 18 to 35 ± 6 nm respectively ($W_{E10S} > W_{E12S}$). The W/H aspect ratio decreased with increasing hydrolysis time, with an average of approximately 4 ± 1 (except for E2S sample, W/H=8). L/W aspect ratios had an average between 3.7 and 13, and tend to decrease with higher acid concentrations. While the calculated L/H aspect ratios are between 16-43 and, are higher for the low acid concentration, time, and temperatures as shown in Table S5.

CNC-S with aspect ratios between 10 to 45 have proven useful for their use as reinforcement materials [10]. A complete comparison from different natural fibers and other raw materials is shown in Table 6, which shows that due to the similar conditions used in this article, there is no difference between the raw materials used to generate CNC-S and the conditions are more important to obtain specific dimensions. The L/D aspect ratio reported in this work is based on the CNC height.

Preprints (www.preprints.org) | NOT PEER-REVIEWED | Posted: 28 January 2021 doi:10.20944/preprints202101.0586.v1

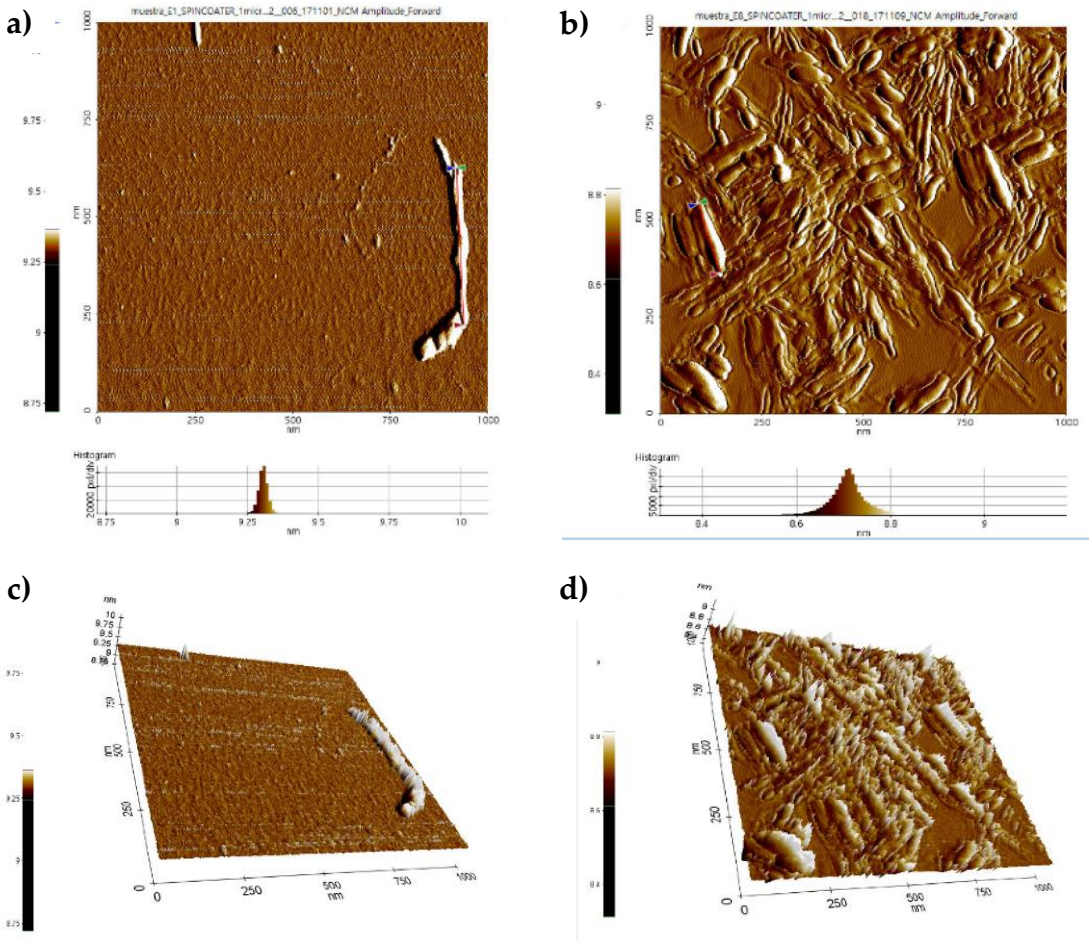

Figure 6. AFM images of CNC-S for two different conditions: (**a**) 2D image and histogram of E1S, (**b**) 2D image and histogram of E8S, (**c**) 3D image of E1S, (**d**) 3D image of E8S.

For most cellulose nanomaterials, whether they are nanocrystals, nanofibers, nanowhiskers, etc., L/D of 20 or more is mentioned [58], so the aspect ratios obtained in this work for sulfuric acid meet for the L/H ratio, the L/W aspect ratios are between 5 and 11 while the W/H aspect ratios are approximately 4 ± 1 for most samples.

Different CNC-S morphologies obtained from cotton by hydrolysis with H_2SO_4, have been reported by Lin and Dufresne (2014) [26], which include circular and ellipsoidal cylindrical shapes as well as flat or laminar shapes, their results probe that sulfation degree is related to CNC-S morphology, particularly on cross-section which corresponds to an ellipsoid model. Our results showed that the cross-section of the CNC-S is wider than its high (W > H), which corresponds more to an ellipsoidal shape. The dimensions changes with hydrolysis time, temperature, and acid concentration, so this behavior should be attributed to the total sulfate groups in the CNC-S. This suggests that, as the content of total sulfate groups in the CNC-S increases, W decreases, that is, the surface charge increases and prevents interactions between the nanocrystals attributed to the hydrogen bonds of the OH groups, thus reducing the agglomerations of the CNC-S, so that W can be directly related to the agglomerations and it could be due to absence of sulfate groups in the CNC-H.

Table 5. Dimension comparison of CNC-S from different raw sources.

Source	Conditions	Diameter (nm)	Length (nm)	L/D	Reference

Preprints (www.preprints.org) | NOT PEER-REVIEWED | Posted: 28 January 2021 doi:10.20944/preprints202101.0586.v1

***Agave tequilana* Weber var. Azul**	All	8.7-9.3	137-404	14.7-44.4	This work
	E1S (60 wt%, 40°C, 40 min)	9.3	404	43.4	
	E8S (65 wt% N, 60°C, 70 min)	9.2	149	16.2	
Agave angustifolia	60 wt%, 45°C, 45 min	8 - 15	170 - 500	10 - 45	[11]
Agave sisalana	55 wt%, 45-60°C, 20-30 min	5.9 – 10.5	177 - 433	14 - 15	[59]
Agave tequilana	65 wt%, 50°C, 60 min	11	323 ± 112	28	[9]
Barley	65 wt%, 50°C, 60 min	10	329 ± 123	32	[9]
MCC	64 wt%, 44°C, 130 min	16	218 ± 56	13	[9]
MCC	50°C, 60 min	14-16	200-250	14-15	[18]
***Acacia farnesiana* L. Willd**	60-65 %, 45-55 ºC, 45-65 min	-	100-260	-	[27]

3.6. Zeta potential, Dynamic Light Scattering (DLS) and Atomic force microscopy (AFM) comparison

To determine the stability of the solutions, Z-potential measurements were made as an indicator of the degree of electrostatic repulsion between the charges of the dispersion particles. Particles with absolute values in the 40-60 mV range show stability, while those with absolute values lower than 30 mV tend to aggregate [60]. The average Z-potential of CNC-S (E1S) showed values of -54.1 ± 6.2 mV, which is considered stable, due to the presence of negative sulfate groups on the surface. For CNC-H (E1H), the average Z potential value was -25.1 ± 8.9 mV. In terms of stability, CNC-H had lower stability than CNC-S, due to the presence of OH groups on the surface, as observed by AFM These results suggest that the CNC-H obtained by hydrolysis with HCl will show a greater tendency to agglomerate (Figures 6 and S3).

The CNC particle size obtained by DLS was compared to the length values obtained by AFM, for both acid hydrolysis. The CNC morphology and the aspect ratio are also discussed as a function of the type of acid and hydrolysis conditions. The complete list of values of the hydrodynamic diameter (d.nm) and the PdI are shown in Tables S1 and S2.

Figure 8a shows the particle size distribution obtained by DLS for CNC-H corresponding to sample E6H. The rest of CNC-H samples showed a similar size distribution behavior, which corresponded to a Gaussian type, with a unimodal distribution. For these samples, the polydispersity index (PdI) was on average 0.32 ± 0.09. The smallest value was obtained for the E12H sample with a hydrodynamic diameter of 323 ± 18 nm and a PdI of 0.24 ± 0.06, while the highest value was for the E2H sample with a hydrodynamic diameter of 794 ± 245 nm and a PdI of 0.50 ± 0.22.

The size distributions of the CNC-S showed a monomodal distribution at the lowest limit of temperature (40°C) and time (40 min) for both acid concentrations (60 and 65 wt%, experimental conditions E1S and E2S). The samples showed PDI values of 0.31 and 0.36 for ES1 and ES2, respectively. The experimental setup E4S changed to a bimodal size distribution (Figure 8b), in which two distinctive peaks of 47 ± 16 nm (14 ± 5%), and 370 ± 109 nm (78.7 ± 7%) were observed for the hydrodynamic diameters. In almost all CNC-S samples the first peak represents 10-40% of the signal intensity, with particle sizes between 30 and 100 nm, while the second peak represents 60-90% of the intensity distribu-

Preprints (www.preprints.org) | NOT PEER-REVIEWED | Posted: 28 January 2021 doi:10.20944/preprints202101.0586.v1

tion, with particle sizes between 200-550 nm. Samples are bimodal with PDI average values above 0.66 ± 0.12 and are only presented for comparison reasons [61].

Similar bimodal size distributions were also observed for CNC-S obtained from laser printer paper [62]. The bimodal distribution was due to the presence of different sized fibers in the paper, and it was also attributed to the process applied for obtaining CNC. Whereas, for CNC-H and CNC-S from *Acacia farneciana* L. Willd the bimodal size distribution was suggested to be due to the bleaching process and specific hydrolysis conditions [27]. On the other hand, diprotic acids such as H_2SO_4 produce monovalent and divalent ions (HSO_4^- and $SO_4^=$), and the composition in aqueous systems depends on the concentration and temperature of the system. This suggests that during hydrolysis, both HSO_4^- and $SO_4^=$ ions coexist, which probably can attack pulp in different ways, generating nanocrystals with varied morphologies and dimensions.

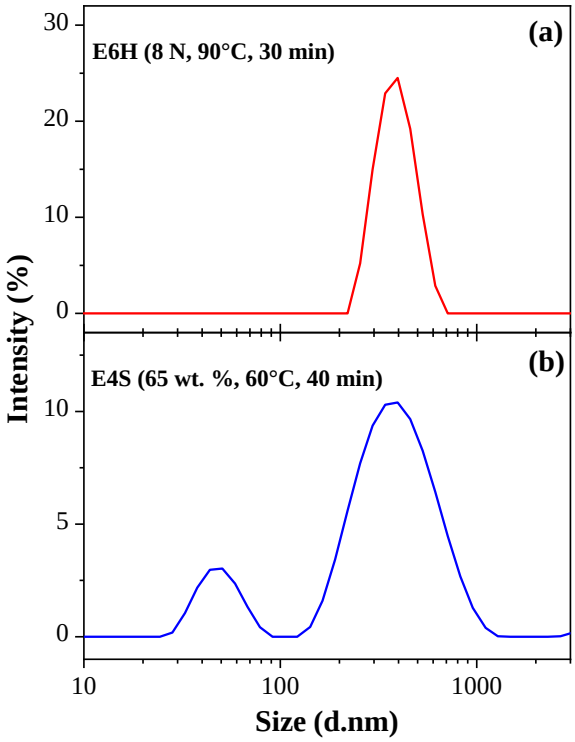

Figure 8. Representative CNC particle size distribution by DLS: (**a**) CNC-H (E6H) y (**b**) CNC-S (E4S).

Figure 9 shows a comparison of the average particle size of the CNC obtained by DLS and AFM. Larger CNC-H particle sizes were obtained (Figure 9a, 300-800 nm), compared to CNC-S (Figure 9b, 100-500 nm). The recorded lengths measured via AFM are relatively similar to the hydrodynamic diameters measured by DLS, which is a faster technique and is usually reported in the literature to estimate the lengths of CNC obtained from different types of raw materials.

HCl concentration was a determining factor in the size of the nanocrystal, obtaining smaller sizes when concentrations were higher (8N) (Figure 9a). In this case, the hydrodynamic diameters oscillated between 300-500 nm for HCl 8 N, except for the lower limits of temperature (50°C) and hydrolysis time (30 min) where the diameter is 829 ± 282 nm. Lower concentrations of HCl (2N) gave higher hydrodynamic diameters of 450-800 nm. Similarly, CNC-H diameter did not rely on the temperature at low concentrations of HCl, with an average size of 570 ± 164 nm. In contrast, at higher HCl concentrations the size decreased with increasing temperature (50 and 90°C) and hydrolysis time. Hydrolysis with H_2SO_4 gave smaller hydrodynamic diameters than those obtained with HCl (Figure 9b). The size values reported in this graph correspond to the average size from

Preprints (www.preprints.org) | NOT PEER-REVIEWED | Posted: 28 January 2021 doi:10.20944/preprints202101.0586.v1

their bimodal distribution, which is more inclined to the longer length of elongated ellipsoids as demonstrated by AFM.

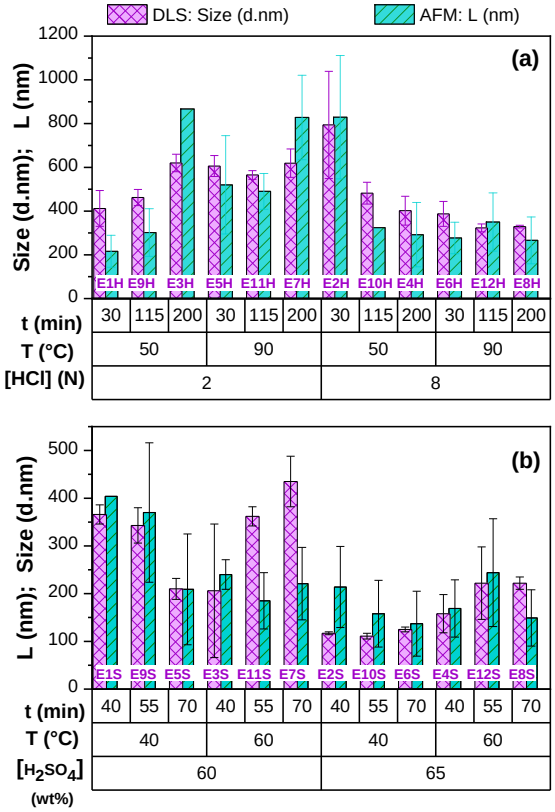

Figure 9. CNC length comparison measured using AFM and DLS for both acid hydrolysis: (**a**) CNC-H (**b**) CNC-S.

Figure 10 shows the effect of the hydrolysis conditions with HCl (Figure 10a), and H_2SO_4 60 and 65 wt% (Figure 10b) on the CNC length measured with AFM.

In Figure 10a, CNC smaller crystals can be obtained at higher acid concentrations (8 N), with length values between 270-350 nm, except for E2H (829 ± 282 nm). For lower HCl concentrations (2N), CNC-H length values increased with hydrolysis time (from 200 to 800 nm). A correlation with temperature was not observed. The Pareto analysis (Figure 11a) revealed that concentration and time (AC) was the only statistically significant negative interaction reflecting an inverse relationship, which was also visualized in the 3D representation.

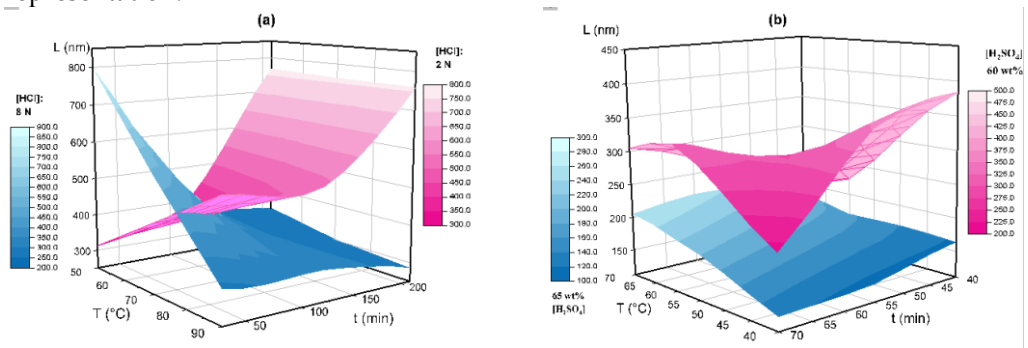

Figure 10. 3D representation of lengths measured by AFM for temperature, time, and different acid conditions: (**a**) HCl hydrolysis, 8N (blue) and 2N (magenta); (**b**) H2SO4 hydrolysis, 65 wt% (blue) and 60 wt% (magenta).

The recorded lengths for CNC-S (Figure 10b) are located between two surfaces delimited by acid concentration. For 65 wt% H_2SO_4, lengths are in the range of 140-250 nm, while for lower concentrations, the length is in the range of 200-400 nm. A non-linear

Preprints (www.preprints.org) | NOT PEER-REVIEWED | Posted: 28 January 2021 doi:10.20944/preprints202101.0586.v1

dependence with time and temperature was also observed. The Pareto analysis (Figure 11b) showed that concentration was the only statistically significant factor contributing to CNC-S length.

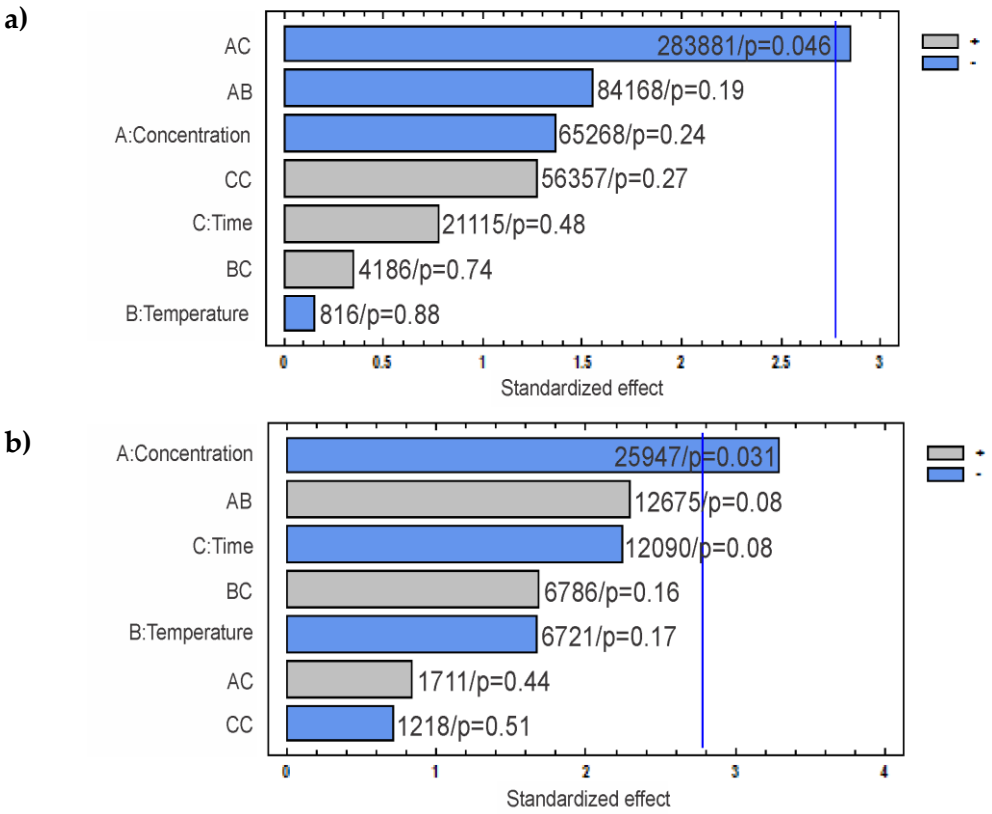

Figure 11. (**a**) Pareto standardized effect for CNC-H length measured by AFM; (**b**) Pareto standardized effect for CNC-S length measured by AFM. The sum of squares and p-value is shown at the right side of each bar.

5. Conclusions

- CNC were successfully obtained from soluble-grade cellulose pulp from *A. tequilana* Weber var. Azul bagasse using an experimental design 2^3 for two acids, H_2SO_4 and HCl. The use of *A. tequilana* bagasse as a raw material is an alternative use to a waste sub-product.
- The maximum CNC yield was 90 and 96% for CNC-H and CNC-S, respectively, for the most severe hydrolysis conditions tested.
- For CNC-S, the total sulfate group content measured followed an exponential behavior as a function of time: $C_{SG} = Ct * \frac{V_2}{m}$. The C_{SG} increased with hydrolysis time, temperature, and H_2SO_4 concentration. The C_{SG} values ranged from 10 to 150 mmol/kg, depending on the hydrolysis conditions.
- The insertion of sulfate groups on CNC-S was also corroborated using XPS, and the results showed 4.92% of sulfate groups for E1S sample. The presence of sulfate groups on CNC-S was also detected by FTIR.
- The FTIR spectra showed LOI and TOI similar to those of soluble-grade cellulose pulp, near to 1 in both cases (1.03 ± 0.17 and 1.00 ± 0.13 respectively), while HBI increased about 30%.
- The CNC crystallinity was obtained by XRD using the Rietveld method. For all the analyzed samples, the crystallinity values ranged from to 88.4 to 91.3%, while the value for soluble grade cellulose pulp was 79.2%

- The Pareto analysis revealed that HCl concentration and time factor interaction (AC) is statistically significant on CNC-H length, whereas H_2SO_4 concentration is the only statistically significant factor for CNC-S length.
- The CNC lengths obtained by AFM are very similar to the diameter (d.nm) obtained using DLS.
- The CNC-S lengths were shorter and thinner than those of CNC-H, probably attributed to sulfate group insertion.
- The smallest CNC-H was observed with 8N HCl (266-350 nm, with the exception of sample E2H), and the longest CNC-H was obtained with 2N HCl (256-867 nm). The smallest CNC-S was obtained with 65 wt% H_2SO_4 (137-244 nm) and the longest CNC-S was obtained with 60 wt.% H_2SO_4 (185-404 nm).

Supplementary Materials: Figure S1. (a) Pareto standardized effect for CNC-H yield production; (b) Pareto standardized effect for CNC-S yield production. The sum of squares and p-value is shown at the right side of each bar; Figure S2. Rietveld analysis for (a) CNC-S (E3S), (b) CNC-H (E10H); Figure S3. AFM 2D images of the 12 CNC-H samples; Figure S4. AFM 2D images of the 12 CNC-S samples; Table S1. DLS and yield results for CNC-H production; Table S2. DLS and yield results for CNC-S production; Table S3. Total sulfate groups of CNC-S; Table S4. AFM measurements of CNC-H; Table S5. AFM measurements of CNC-S

Author Contributions: Conceptualization, J.A.H., and S.G.E; methodology, M.A.G.S., and E.R.B.M.; software, R.R.C.; validation, E.R.B.M.; formal analysis, M.A.G.S., T.D.V, L.C.R.R., and E.R.M.B.; investigation, M.A.G.S., A.B.N.H., R.R.C. and E.B.F.O.; resources, J.F.A.S.M.; data curation, M.A.G.S., T.D.V, L.C.R.R., and E.R.M.B.; writing—original draft preparation, M.A.G.S., T.D.V, L.C.R.R., and E.R.M.B.; writing—review and editing, M.A.G.S., T.D.V, L.C.R.R., and E.R.M.B.; visualization, E-R.M.B., and J.F.A.S.M; supervision, E.R.M.B., and J.F.A.S.M ; project administration, E.R.M.B., and J.F.A.S.M; funding acquisition, E.R.M.B., J.A.H., and J.F.A.S.M. All authors have read and agreed to the published version of the manuscript.

Funding: The authors are grateful for the support of the Consejo Nacional de Ciencia y Tecnología (CONACyT), Grant No. 334914 (CVU: 632616). The authors also would like to acknowledge the Secretaría de Educación Pública for its support at the beginning of this work with the project: "Development and innovation in nanomaterials and nanocomposites, from the International Thematic Network", call 2015.

Conflicts of Interest: The authors declare no conflict of interest.

References

1. Grishkewich, N.; Mohammed, N.; Tang, J.; Tam, K.C. Recent advances in the application of cellulose nanocrystals. *Curr. Opin. Colloid Interface Sci.* 2017, *29*, 32–45.
2. Lin, N.; Dufresne, A. Nanocellulose in biomedicine: Current status and future prospect. *Eur. Polym. J.* **2014**, *59*, 302–325, doi:10.1016/j.eurpolymj.2014.07.025.
3. Yu, H.; Qin, Z.; Liang, B.; Liu, N.; Zhou, Z.; Chen, L. Facile extraction of thermally stable cellulose nanocrystals with a high yield of 93% through hydrochloric acid hydrolysis under hydrothermal conditions. *J. Mater. Chem. A* **2013**, *1*, 3938–3944, doi:10.1039/c3ta01150j.
4. Leung, A.C.W.; Lam, E.; Chong, J.; Hrapovic, S.; Luong, J.H.T. Reinforced plastics and aerogels by nanocrystalline cellulose. *J. Nanoparticle Res.* 2013, *15*, 1–24.
5. Azizi Samir, M.A.S.; Alloin, F.; Sanchez, J.Y.; Dufresne, A. Cellulose nanocrystals reinforced poly(oxyethylene). *Polymer (Guildf).* **2004**, *45*, 4149–4157, doi:10.1016/j.polymer.2004.03.094.
6. Brinchi, L.; Cotana, F.; Fortunati, E.; Kenny, J.M. Production of nanocrystalline cellulose from lignocellulosic biomass: Technology and applications. *Carbohydr. Polym.* 2013, *94*, 154–169.
7. Mohammadkazemi, F.; Doosthoseini, K.; Ganjian, E.; Azin, M. Manufacturing of bacterial nano-cellulose reinforced fiber-cement composites. *Constr. Build. Mater.* **2015**, *101*, 958–964, doi:10.1016/j.conbuildmat.2015.10.093.

8. Jemaa, N.; Paleologou, M.; Zhang, X.; Repoit, I.S. Fractionation of a waste liquor stream from nanocrystalline cellulose production. (US8709203B2) 2009, *2*, 23pp.
9. Espino, E.; Cakir, M.; Domenek, S.; Román-Gutiérrez, A.D.; Belgacem, N.; Bras, J. Isolation and characterization of cellulose nanocrystals from industrial by-products of Agave tequilana and barley. *Ind. Crops Prod.* **2014**, *62*, 552–559, doi:10.1016/j.indcrop.2014.09.017.
10. Dhar, P.; Bhasney, S.M.; Kumar, A.; Katiyar, V. Acid functionalized cellulose nanocrystals and its effect on mechanical, thermal, crystallization and surfaces properties of poly (lactic acid) bionanocomposites films: A comprehensive study. *Polymer (Guildf).* **2016**, *101*, 75–92, doi:10.1016/j.polymer.2016.08.028.
11. Rosli, N.A.; Ahmad, I.; Abdullah, I. Isolation and characterization of cellulose nanocrystals from agave angustifolia fibre. *BioResources* **2013**, *8*, 1893–1908, doi:10.15376/biores.8.2.1893-1908.
12. Roman, M.; Winter, W.T. Effect of sulfate groups from sulfuric acid hydrolysis on the thermal degradation behavior of bacterial cellulose. *Biomacromolecules* **2004**, *5*, 1671–1677, doi:10.1021/bm034519+.
13. Dong, X.M.; Revol, J.F.; Gray, D.G. Effect of microcrystallite preparation conditions on the formation of colloid crystals of cellulose. *Cellulose* **1998**, *5*, 19–32, doi:10.1023/A:1009260511939.
14. Beck-Candanedo, S.; Roman, M.; Gray, D.G. Effect of Reaction Conditions on the Properties and Behavior of Wood Cellulose Nanocrystal Suspensions. *Biomacromolecules* **2005**, *6*, 1048–1054, doi:10.1021/bm049300p.
15. Elazzouzi-Hafraoui, S.; Nishiyama, Y.; Putaux, J.-L.; Heux, L.; Dubreuil, F.; Rochas, C. The Shape and Size Distribution of Crystalline Nanoparticles Prepared by Acid Hydrolysis of Native Cellulose. *Biomacromolecules* **2008**, *9*, 57–65, doi:10.1021/bm700769p.
16. Cheng, M.; Qin, Z.; Chen, Y.; Hu, S.; Ren, Z.; Zhu, M. Efficient Extraction of Cellulose Nanocrystals through Hydrochloric Acid Hydrolysis Catalyzed by Inorganic Chlorides under Hydrothermal Conditions. *ACS Sustain. Chem. Eng.* **2017**, *5*, 4656–4664, doi:10.1021/acssuschemeng.6b03194.
17. Montanari, S.; Roumani, M.; Heux, L.; Vignon, M.R. Topochemistry of Carboxylated Cellulose Nanocrystals Resulting from TEMPO-Mediated Oxidation. *Macromolecules* **2005**, *38*, 1665–1671, doi:10.1021/ma048396c.
18. Yu, H.Y.; Qin, Z.Y.; Liu, L.; Yang, X.G.; Zhou, Y.; Yao, J.M. Comparison of the reinforcing effects for cellulose nanocrystals obtained by sulfuric and hydrochloric acid hydrolysis on the mechanical and thermal properties of bacterial polyester. *Compos. Sci. Technol.* **2013**, *87*, 22–28, doi:10.1016/j.compscitech.2013.07.024.
19. Yu, H.Y.; Qin, Z.Y.; Sun, B.; Yan, C.F.; Yao, J.M. One-pot green fabrication and antibacterial activity of thermally stable corn-like CNC/Ag nanocomposites. *J. Nanoparticle Res.* **2014**, *16*, 1–12, doi:10.1007/s11051-013-2202-4.
20. Consejo Regulador del Tequila Available online: https://www.crt.org.mx/EstadisticasCRTweb/ (accessed on Oct 1, 2020).
21. Huitrón, C.; Pérez, R.; Sánchez, A.; Lappe, P.; Zavaleta, L.R. Agricultural waste from the tequila industry as substrate for the production of commercially important enzymes. *J. Environ. Biol.* **2008**, *1*, 37–41.
22. Gallardo-Sánchez, M.A.; Hernández, J.A.; Casillas, R.R.; Vázquez, J.I.E.; Hernández, D.E.; Martínez, J.F.A.S.; Enríquez, S.G.; Balleza, E.R.M. Obtaining Soluble-grade cellulose pulp from Agave tequilana Weber var. Azul Bagasse. *BioResources* **2019**, *14*, 9867–9881, doi:10.15376/biores.14.4.9867-9881.
23. Ponce-Reyes, C.E.; Chanona-Pérez, J.J.; Garibay-Febles, V.; Palacios-González, E.; Karamath, J.; Terrés-Rojas, E.; Calderón-Domínguez, G. Preparation of cellulose nanoparticles from agave waste and its morphological and structural characterization. *Rev. Mex. Ing. Quim.* **2014**, *13*, 897–906.
24. Pech-Cohuo, S.C.; Canche-Escamilla, G.; Valadez-González, A.; Fernández-Escamilla, V.V.A.; Uribe-Calderon, J. Production and Modification of Cellulose Nanocrystals from Agave tequilana Weber Waste and Its Effect on the Melt Rheology of PLA. *Int. J. Polym. Sci.* **2018**, *2018*, doi:10.1155/2018/3567901.
25. Lu, H.; Gui, Y.; Zheng, L.; Liu, X. Morphological, crystalline, thermal and physicochemical properties of cellulose nanocrystals obtained from sweet potato residue. *Food Res. Int.* **2013**, *50*, 121–128, doi:10.1016/j.foodres.2012.10.013.

26. Lin, N.; Dufresne, A. Surface chemistry, morphological analysis and properties of cellulose nanocrystals with gradiented sulfation degrees. *Nanoscale* **2014**, *6*, 5384–5393, doi:10.1039/C3NR06761K.
27. Ramírez Casillas, R.; López López, M. del C.; Becerra Aguilar, B.; Dávalos Olivares, F.; Satyanarayana, K.G. Preparation and characterization of cellulose nanocrystals using soluble grade cellulose from acid hydrolysis of Huizache (Acacia farnesiana L. Willd.). *BioResources* **2019**, *14*, 3319–3338, doi:10.15376/biores.14.2.3319-3338.
28. Elhalil, A.; Tounsadi, H.; Elmoubarki, R.; Mahjoubi, F.Z.; Farnane, M.; Sadiq, M.; Abdennouri, M.; Qourzal, S.; Barka, N. Factorial experimental design for the optimization of catalytic degradation of malachite green dye in aqueous solution by Fenton process. *Water Resour. Ind.* **2016**, *15*, 41–48, doi:10.1016/j.wri.2016.07.002.
29. Erper, I.; Turkkan, M.; Odabas, M.S. The mathematical approach to the effect of potassium bicarbonate on mycelial growth of Sclerotinia sclerotiorum and Rhizoctonia solani in vitro. **2011**, *98*, 195–204.
30. Filson, P.B.; Dawson-Andoh, B.E. Sono-chemical preparation of cellulose nanocrystals from lignocellulose derived materials. *Bioresour. Technol.* **2009**, *100*, 2259–2264, doi:10.1016/j.biortech.2008.09.062.
31. Bondeson, D.; Mathew, A.; Oksman, K. Optimization of the isolation of nanocrystals from microcrystalline cellulose by acid hydrolysis. *Cellulose* **2006**, *13*, 171–180, doi:10.1007/s10570-006-9061-4.
32. Ramirez Casillas, R.; López López, M. del C.; Becerra Aguilar, B.; Dávalos Olivares, F.; Gundapa Satyanarayana, K. Obtaining dissolving grade cellulose from the huizache (Acacia farnesiana L. Willd.) plant. *BioResources* **2019**, *14*, 3301–3318, doi:10.15376/biores.14.2.3301-3318.
33. Vickerman, J.C.; Gilmore, I.S. *Surface Analysis– The Principal Techniques*; Vickerman, J.C., Gilmore, I.S., Eds.; John Wiley & Sons, Ltd: Chichester, UK, 2009; ISBN 9780470721582.
34. Snyder, R.L. Analytical profile fitting of X-ray powder diffraction profiles in Rietveld analysis. In *The Rietveld Method*; 1993; Vol. 1, pp. 111–131 ISBN 0198555776.
35. Antoy, J. *Design of Experiments for Engineers and Scientists: Second Edition*; Elsevier Ltd, 2014; ISBN 9780080994178.
36. Beamson, G.; Briggs, D. *High resolution XPS of organic polymers: the scienta ESCA300 database*; John Wiley & Sons, 1992; ISBN 0471935921.
37. Xu, F.; Yu, J.; Tesso, T.; Dowell, F.; Wang, D. Qualitative and quantitative analysis of lignocellulosic biomass using infrared techniques: A mini-review. *Appl. Energy* 2013, *104*, 801–809.
38. Robles, E.; Fernández-Rodríguez, J.; Barbosa, A.M.; Gordobil, O.; Carreño, N.L.V.; Labidi, J. Production of cellulose nanoparticles from blue agave waste treated with environmentally friendly processes. *Carbohydr. Polym.* **2018**, *183*, 294–302, doi:10.1016/j.carbpol.2018.01.015.
39. Anwar, B.; Bundjali, B.; Arcana, I.M. Isolation of Cellulose Nanocrystals from Bacterial Cellulose Produced from Pineapple Peel Waste Juice as Culture Medium. *Procedia Chem.* **2015**, *16*, 279–284, doi:10.1016/j.proche.2015.12.051.
40. Contreras, H.J.; Trujillo, H.A.; Arias, G.; Pérez, J.; Delgado, E. Espectroscopia Atr-Ftir De Celulosa: Aspecto Instrumental Y Tratamiento Matemático De Espectros. *e-Gnosis* **2010**, *8*, 1–13.
41. O'Connor, R.T.; DuPré, E.F.; Mitcham, D. Applications of Infrared Absorption Spectroscopy to Investigations of Cotton and Modified Cottons. *Text. Res. J.* **1958**, *28*, 382–392, doi:10.1177/004051755802800503.
42. Lu, P.; Hsieh, Y.-L. Preparation and characterization of cellulose nanocrystals from rice straw. *Carbohydr. Polym.* **2012**, *87*, 564–573, doi:10.1016/j.carbpol.2011.08.022.
43. Poletto, M.; Ornaghi, H.; Zattera, A. Native Cellulose: Structure, Characterization and Thermal Properties. *Materials (Basel).* **2014**, *7*, 6105–6119, doi:10.3390/ma7096105.
44. Oh, S.Y.; Yoo, D. Il; Shin, Y.; Kim, H.C.; Kim, H.Y.; Chung, Y.S.; Park, W.H.; Youk, J.H. Crystalline structure analysis of cellulose treated with sodium hydroxide and carbon dioxide by means of X-ray diffraction and FTIR spectroscopy. *Carbohydr. Res.* **2005**, *340*, 2376–2391, doi:10.1016/j.carres.2005.08.007.
45. Kumar, A.; Singh Negi, Y.; Choudhary, V.; Kant Bhardwaj, N. Characterization of Cellulose Nanocrystals Produced by

Acid-Hydrolysis from Sugarcane Bagasse as Agro-Waste. *J. Mater. Phys. Chem.* **2020**, *2*, 1–8, doi:10.12691/jmpc-2-1-1.

46. Kruer-Zerhusen, N.; Cantero-Tubilla, B.; Wilson, D.B. Characterization of cellulose crystallinity after enzymatic treatment using Fourier transform infrared spectroscopy (FTIR). *Cellulose* **2018**, *25*, 37–48, doi:10.1007/s10570-017-1542-0.
47. Hurtubise, F.G.; KrÄSSIG, H. Classification of Fine Structural Characteristics in Cellulose by Infrared Spectroscopy Use of Potassium Bromide Pellet Technique. *Anal. Chem.* **1960**, *32*, 177–181, doi:10.1021/ac60158a010.
48. Carrillo, F.; Colom, X.; Suñol, J..; Saurina, J. Structural FTIR analysis and thermal characterisation of lyocell and viscose-type fibres. *Eur. Polym. J.* **2004**, *40*, 2229–2234, doi:10.1016/j.eurpolymj.2004.05.003.
49. Nelson, M.L.; O'Connor, R.T. Relation of certain infrared bands to cellulose crystallinity and crystal lattice type. Part II. A new infrared ratio for estimation of crystallinity in celluloses I and II. *J. Appl. Polym. Sci.* **1964**, *8*, 1325–1341, doi:10.1002/app.1964.070080323.
50. Nelson, M.L.; O'Connor, R.T. Relation of certain infrared bands to cellulose crystallinity and crystal latticed type. Part I. Spectra of lattice types I, II, III and of amorphous cellulose. *J. Appl. Polym. Sci.* **1964**, *8*, 1311–1324, doi:10.1002/app.1964.070080322.
51. Mariano, M.; El Kissi, N.; Dufresne, A. Cellulose nanocrystals and related nanocomposites: Review of some properties and challenges. *J. Polym. Sci. Part B Polym. Phys.* **2014**, *52*, 791–806, doi:10.1002/polb.23490.
52. Tronc, E.; Hernández-Escobar, C.A.; Ibarra-Gómez, R.; Estrada-Monje, A.; Navarrete-Bolaños, J.; Zaragoza-Contreras, E.A. Blue agave fiber esterification for the reinforcement of thermoplastic composites. *Carbohydr. Polym.* **2007**, *67*, 245–255, doi:10.1016/j.carbpol.2006.05.027.
53. Popa, N.C.; Balzar, D. Size-broadening anisotropy in whole powder pattern fitting. Application to zinc oxide and interpretation of the apparent crystallites in terms of physical models. *J. Appl. Crystallogr.* **2008**, *41*, 615–627, doi:10.1107/S0021889808012223.
54. De Figueiredo, L.P.; Ferreira, F.F. The Rietveld Method as a Tool to Quantify the Amorphous Amount of Microcrystalline Cellulose. *J. Pharm. Sci.* **2014**, *103*, 1394–1399, doi:10.1002/jps.23909.
55. Chen, L.; Wang, Q.; Hirth, K.; Baez, C.; Agarwal, U.P.; Zhu, J.Y. Tailoring the yield and characteristics of wood cellulose nanocrystals (CNC) using concentrated acid hydrolysis. *Cellulose* **2015**, *22*, 1753–1762, doi:10.1007/s10570-015-0615-1.
56. Lomelí-Ramírez, M.G.; Valdez-Fausto, E.M.; Rentería-Urquiza, M.; Jiménez-Amezcua, R.M.; Anzaldo Hernández, J.; Torres-Rendon, J.G.; García Enriquez, S. Study of green nanocomposites based on corn starch and cellulose nanofibrils from Agave tequilana Weber. *Carbohydr. Polym.* **2018**, *201*, 9–19, doi:10.1016/j.carbpol.2018.08.045.
57. Naseri, N.; Mathew, A.P.; Girandon, L.; Fröhlich, M.; Oksman, K. Porous electrospun nanocomposite mats based on chitosan–cellulose nanocrystals for wound dressing: effect of surface characteristics of nanocrystals. *Cellulose* **2015**, *22*, 521–534, doi:10.1007/s10570-014-0493-y.
58. Rosa, M.F.; Medeiros, E.S.; Malmonge, J.A.; Gregorski, K.S.; Wood, D.F.; Mattoso, L.H.C.; Glenn, G.; Orts, W.J.; Imam, S.H. Cellulose nanowhiskers from coconut husk fibers: Effect of preparation conditions on their thermal and morphological behavior. *Carbohydr. Polym.* **2010**, *81*, 83–92, doi:10.1016/j.carbpol.2010.01.059.
59. Siqueira, G.; Tapin-Lingua, S.; Bras, J.; da Silva Perez, D.; Dufresne, A. Morphological investigation of nanoparticles obtained from combined mechanical shearing, and enzymatic and acid hydrolysis of sisal fibers. *Cellulose* **2010**, *17*, 1147–1158, doi:10.1007/s10570-010-9449-z.
60. Hanaor, D.; Michelazzi, M.; Leonelli, C.; Sorrell, C.C. The effects of carboxylic acids on the aqueous dispersion and electrophoretic deposition of ZrO2. *J. Eur. Ceram. Soc.* **2012**, *32*, 235–244, doi:10.1016/j.jeurceramsoc.2011.08.015.
61. Standardization, I.O. for Particle size analysis-dynamic light scattering (DLS) (ISO 22412) 2017.
62. Ramírez Casillas, R.; Báez Rodríguez, K.F.; Cruz-Estrada, R.H.; Dávalos-Olivares, F.; Navarro-Arzate, F.; Satyanarayana, K.G. Isolation and Characterization of Cellulose Nanocrystals Created from Recycled Laser Printed Paper. *BioResources* **2018**, *13*, doi:10.15376/biores.13.4.7404-7429.

 doi:10.20944/preprints202101.0586.v1